Generalized Jones matrix optical coherence tomography: performance and local birefringence imaging

Shuichi Makita*, Masahiro Yamanari, and Yoshiaki Yasuno

Computational Optics Group in University of Tsukuba, 1-1-1 Tennodai, Tsukuba, Ibaraki 305-8573, Japan

makita@optlab2.bk.tsukuba.ac.jp

http://optics.bk.tsukuba.ac.jp/COG/

Abstract: Phase retardation imaging including local birefringence imaging of biological tissues is described by generalized Jones-matrix optical coherence tomography. The polarization properties of a local tissue can be obtained from two Jones matrices that are measured by backscattered lights from the front and back boundaries of the local tissue. The error in the phase retardation measurement due to background noise is analyzed theoretically, numerically, and experimentally. The minimum detectable phase retardation is estimated from numerical simulations. The theoretical analysis suggests that the measurements with two orthogonal input polarization states have the lowest retardation error. Local birefringence imaging is applied to the human anterior eye chamber and skin *in vivo*.

© 2010 Optical Society of America

OCIS codes: (170.4500) Optical coherence tomography; (120.5410) Polarimetry; (260.1440); (260.5430) Polarization Birefringence; (170.4470) Ophthalmology; (170.1870) Dermatology.

References and links

1. D. Huang, E. A. Swanson, C. P. Lin, J. S. Schuman, W. G. Stinson, W. Chang, M. R. Hee, T. Flotte, K. Gregory, C. A. Puliafito, and J. G. Fujimoto, "Optical coherence tomography," Science **254**, 1178–1181 (1991).
2. J. S. Schuman, M. R. Hee, C. A. Puliafito, C. Wong, T. Pedut-Kloizman, C. P. Lin, E. Hertzmark, J. A. Izatt, E. A. Swanson, and J. G. Fujimoto, "Quantification of nerve fiber layer thickness in normal and glaucomatous eyes using optical coherence tomography," Arch. Ophthalmol. **113**, 586–596 (1995).
3. G. J. Tearney, M. E. Brezinski, S. A. Boppart, B. E. Bouma, N. Weissman, J. F. Southern, E. A. Swanson, and J. G. Fujimoto, "Images in cardiovascular medicine. Catheter-based optical imaging of a human coronary artery," Circulation **94**, 3013 (1996).
4. J. Welzel, E. Lankenau, R. Birngruber, and R. Engelhardt, "Optical coherence tomography of the human skin," J. Am. Acad. Dermatol. **37**, 958–963 (1997).
5. M. R. Hee, D. Huang, E. A. Swanson, and J. G. Fujimoto, "Polarization-sensitive low-coherence reflectometer for birefringence characterization and ranging," J. Opt. Soc. Am. B **9**, 903–908 (1992).
6. B. Cense, T. C. Chen, B. H. Park, M. C. Pierce, and J. F. de Boer, "Thickness and birefringence of healthy retinal nerve fiber layer tissue measured with polarization-sensitive optical coherence tomography," Invest. Ophthalmol. Vis. Sci. **45**, 2606–2612 (2004).
7. M. Yamanari, M. Miura, S. Makita, T. Yatagai, and Y. Yasuno, "Phase retardation measurement of retinal nerve fiber layer by polarization-sensitive spectral-domain optical coherence tomography and scanning laser polarimetry," J. Biomed. Opt. **13**, 014013 (2008).
8. E. Götzinger, M. Pircher, B. Baumann, C. Hirn, C. Vass, and C. K. Hitzenberger, "Retinal nerve fiber layer birefringence evaluated with polarization sensitive spectral domain OCT and scanning laser polarimetry: A comparison," J. Biophoton. **1**, 129–139 (2008).

#118929 - $15.00 USD Received 22 Oct 2009; revised 21 Dec 2009; accepted 23 Dec 2009; published 6 Jan 2010
(C) 2010 OSA

9. S. D. Giattina, B. K. Courtney, P. R. Herz, M. Harman, S. Shortkroff, D. L. Stamper, B. Liu, J. G. Fujimoto, and M. E. Brezinski, "Assessment of coronary plaque collagen with polarization sensitive optical coherence tomography (PS-OCT)," Int. J. Cardiol. **107**, 400–409 (2006).
10. S. K. Nadkarni, M. C. Pierce, B. H. Park, J. F. de Boer, P. Whittaker, B. E. Bouma, J. E. Bressner, E. Halpern, S. L. Houser, and G. J. Tearney, "Measurement of Collagen and Smooth Muscle Cell Content in Atherosclerotic Plaques Using Polarization-Sensitive Optical Coherence Tomography," J. Am. Coll. Cardiol. **49**, 1474–1481 (2007).
11. S. Guo, J. Zhang, L. Wang, J. S. Nelson, and Z. Chen, "Depth-resolved birefringence and differential optical axis orientation measurements with fiber-based polarization-sensitive optical coherence tomography," Opt. Lett. **29**, 2025–2027 (2004).
12. M. Todorović, S. Jiao, L. V. Wang, and G. Stoica, "Determination of local polarization properties of biological samples in the presence of diattenuation by use of Mueller optical coherence tomography," Opt. Lett. **29**, 2402–2404 (2004).
13. N. Kemp, H. Zaatari, J. Park, H. G. R. III, and T. Milner, "Depth-resolved optic axis orientation in multiple layered anisotropic tissues measured with enhanced polarization-sensitive optical coherence tomography (EPS-OCT)," Opt. Express **13**, 4507–4518 (2005). URL http://www.opticsexpress.org/abstract.cfm?URI=oe-13-12-4507.
14. S. Makita, Y. Yasuno, T. Endo, M. Itoh, and T. Yatagai, "Polarization contrast imaging of biological tissues by polarization-sensitive Fourier-domain optical coherence tomography," Appl. Opt. **45**, 1142–1147 (2006).
15. S. Jiao, G. Yao, and L. V. Wang, "Depth-Resolved Two-Dimensional Stokes Vectors of Backscattered Light and Mueller Matrices of Biological Tissue Measured With Optical Coherence Tomography," Appl. Opt. **39**, 6318–6324 (2000).
16. B. H. Park, M. C. Pierce, B. Cense, and J. F. de Boer, "Jones matrix analysis for a polarization-sensitive optical coherence tomography system using fiber-optic components," Opt. Lett. **29**, 2512–2514 (2004).
17. S. Jiao and L. V. Wang, "Jones-matrix imaging of biological tissues with quadruple-channel optical coherence tomography," J. Biomed. Opt. **7**, 350–358 (2002).
18. S.-Y. Lu and R. A. Chipman, "Homogeneous and inhomogeneous Jones matrices," J. Opt. Soc. Am. A **11**, 766 (1994).
19. M. Yamanari, S. Makita, V. Madjarova, T. Yatagai, and Y. Yasuno, "Fiber-based polarization-sensitive Fourier domain optical coherence tomography using B-scan-oriented polarization modulation method," Opt. Express **14**, 6502–6515 (2006). URL http://www.opticsexpress.org/abstract.cfm?id=90792.
20. S. Jiao, W. Yu, G. Stoica, and L. V. Wang, "Optical-fiber-based Mueller optical coherence tomography," Opt. Lett. **28**, 1206–1208 (2003).
21. G. Strang, *Introduction to linear algebra*, 3rd ed. (Wellesley Cambridge Pr, 2003).
22. N. Kemp, H. Zaatari, J. Park, H. G. R. III, and T. Milner, "Form-biattenuance in fibrous tissues measured with polarization-sensitive optical coherence tomography (PS-OCT)," Opt. Express **13**, 4611–4628 (2005). URL http://www.opticsexpress.org/abstract.cfm?URI=oe-13-12-4611.
23. M. Everett, K. Schoenenberger, B. Colston Jr, and L. Da Silva, "Birefringence characterization of biological tissue by use of optical coherence tomography," Opt. Lett. **23**, 228–230 (1998).
24. K. Schoenenberger, B. W. Colston, D. J. Maitland, L. B. D. Silva, and M. J. Everett, "Mapping of Birefringence and Thermal Damage in Tissue by use of Polarization-Sensitive Optical Coherence Tomography," Appl. Opt. **37**, 6026–6036 (1998).
25. M. Yamanari, S. Makita, and Y. Yasuno, "Polarization-sensitive swept-source optical coherence tomography with continuous source polarization modulation," Opt. Express **16**, 5892–5906 (2008). URL http://www.opticsexpress.org/abstract.cfm?URI=oe-16-8-5892.
26. S. Yazdanfar, C. Yang, M. Sarunic, and J. Izatt, "Frequency estimation precision in Doppler optical coherence tomography using the Cramer-Rao lower bound," Opt. Express **13**, 410–416 (2005). URL http://www.opticsexpress.org/abstract.cfm?URI=oe-13-2-410.
27. B. H. Park, M. C. Pierce, B. Cense, S.-H. Yun, M. Mujat, G. J. Tearney, B. E. Bouma, and J. F. de Boer, "Real-time fiber-based multi-functional spectral-domain optical coherence tomography at 1.3 μm," Opt. Express **13**, 3931–3944 (2005). URL http://www.opticsexpress.org/abstract.cfm?id=84093.
28. B. H. Park, M. C. Pierce, B. Cense, and J. F. de Boer, "Optic axis determination accuracy for fiber-based polarization-sensitive optical coherence tomography," Opt. Lett. **30**, 2587–2589 (2005).
29. Y. Yasuno, M. Yamanari, K. Kawana, T. Oshika, and M. Miura, "Investigation of post-glaucoma-surgery structures by three-dimensional and polarization sensitive anterior eye segment optical coherence tomography," Opt. Express **17**, 3980–3996 (2009). URL http://www.opticsexpress.org/abstract.cfm?URI=oe-17-5-3980.
30. S. Sakai, N. Nakagawa, M. Yamanari, A. Miyazawa, Y. Yasuno, and M. Matsumoto, "Relationship between dermal birefringence and the skin surface roughness of photoaged human skin," J. Biomed. Opt. **14**, 044032 2009).
31. D. J. Maitland and J. T. W. Jr., "Quantitative measurements of linear birefringence during heating of native collagen," Lasers. Surg. Med. **20**, 310–318 (1997).

#118929 - $15.00 USD Received 22 Oct 2009; revised 21 Dec 2009; accepted 23 Dec 2009; published 6 Jan 2010
(C) 2010 OSA

32. A. Miyazawa, M. Yamanari, S. Makita, M. Miura, K. Kawana, K. Iwaya, H. Goto, and Y. Yasuno, "Tissue discrimination in anterior eyeusing three optical parameters obtained by polarization sensitive optical coherence tomography," Opt. Express **17**, 17,426–17,440 (2009). URL http://www.opticsexpress.org/abstract.cfm?URI=oe-17-20-17426.
33. M. Miura, M. Yamanari, T. Iwasaki, A. E. Elsner, S. Makita, T. Yatagai, and Y. Yasuno, "Imaging Polarimetry in Age-Related Macular Degeneration," Invest. Ophthalmol. Vis. Sci. **49**, 2661–2667 (2008).
34. C. E. Saxer, J. F. de Boer, B. H. Park, Y. Zhao, Z. Chen, and J. S. Nelson., "High-speed fiber based polarization-sensitive optical coherence tomography of in vivo human skin," Opt. Lett. **25**, 1355–1357 (2000).
35. M. C. Pierce, J. Strasswimmer, B. H. Park, B. Cense, and J. F. D. Boer, "Birefringence measurements in human skin using polarization-sensitive optical coherence tomography," J. Biomed. Opt. **9**, 287–291 (2004).
36. W. Oh, S. Yun, B. Vakoc, M. Shishkov, A. Desjardins, B. Park, J. de Boer, G. Tearney, and B. Bouma, "High-speed polarization sensitive optical frequency domain imaging with frequency multiplexing," Opt. Express **16**, 1096–1103 (2008). URL http://www.opticsexpress.org/abstract.cfm?URI=oe-16-2-1096.
37. M. Yamanari, Y. Lim, S. Makita, and Y. Yasuno, "Visualization of phase retardation of deep posterior eye by polarization-sensitive swept-source optical coherence tomography with1-μm probe," Opt. Express **17**, 12,385–12,396 (2009). URL http://www.opticsexpress.org/abstract.cfm?URI=oe-17-15-12385.

1. Introduction

Optical coherence tomography (OCT) is a high-resolution cross-sectional imaging technique of biological tissues [1]. It has been applied to several clinical applications such as ophthalmology [2], cardiology [3], and dermatology [4]. Its ability to investigate three-dimensional subsurface structures has been widely accepted. On the other hand, the characterization of tissues is essential for interpreting organs and discriminating abnormal tissues. However, the contrast in OCT comprises only scattering intensity. Hence, the discrimination of tissues that have close backscattering is extremely difficult. Additional contrasts for OCT will extend the field of OCT applications.

Polarization-sensitive OCT (PS-OCT) [5] is a promising branch of OCT. PS-OCT can be used to detect fibrous tissues by measuring the changes in the polarization state of light. It shows the applicability for diagnosing glaucoma [6–8] and plaques [9, 10]. However, conventional PS-OCT is not suitable for discriminating fibrous tissues. This is because the phase retardation of light, which is accumulated by passing light through birefringent tissues, is measured and the presence of phase retardation in conventional PS-OCT image does not imply the existence of birefringent tissues. The phase retardation inside birefringent tissues changes, while that in non-birefringent tissues does not change. Hence, the discrimination of birefringent tissues requires the examiner to have considerable experience and some technical knowledge.

Several studies have attempted to resolve the polarization properties of a local site [11–14]. Local phase retardation, which corresponds to the local birefringence of a tissue, can be obtained from accumulated polarization changes at two different axial positions [11]. Since this method does not assume the existence of diattenuation, retardation errors exist when there is diattenuation. In other methods [12, 14], the local polarization properties—retardation and diattenuation—are obtained by peeling off upper layers one by one; however, this requires complex calculus.

Further, it is difficult to determine the local birefringence of a weakly birefringent and weakly scattering tissue. The phase retardation caused by a single layer has to be measured, but the thinner single layer will cause smaller phase retardation. In addition, the low reflectivity of biological samples restricts the signal-to-noise ratio (SNR), and it will affect the contrast of local birefringence images. Hence, it is necessary to investigate the performance of PS-OCT in order to improve local birefringence imaging.

In this paper, we generalize the phase retardation measurement by using Jones matrix OCT and reveal that local birefringence imaging is one part of that. A high-contrast local birefringence imaging method is proposed. The influences of background noises on the phase retar-

#118929 - $15.00 USD Received 22 Oct 2009; revised 21 Dec 2009; accepted 23 Dec 2009; published 6 Jan 2010
(C) 2010 OSA

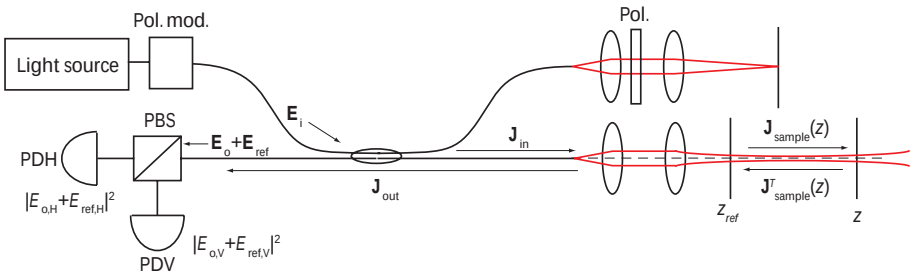

Fig. 1. Schematic diagram of a fiber-based PS-OCT. PDH,PDV, photodetection devices to detect horizontal and vertical polarization components; Pol. mod., polarization modulator; and Pol., polarizer. In the case of time-domain and spectral-domain OCTs, the light source is a broadband light source. It is wavelength-swept light source for swept-source OCT. Photodetection devices are photodetectors for time-domain and swept-source OCTs. They are spectrometers for spectral-domain OCT. Typically the polarizer is introduced in the reference arm to deliver the same optical power of reference beam to two photodetection devices.

dation measurement with Jones matrix OCT is analyzed theoretically and numerically. *In vivo* depth-resolved local birefringence imaging of biological tissues is performed. The optimum pair of incident polarization states from the perspective of background noise is discussed.

2. Theory

2.1. Jones matrix measurement in polarization-sensitive OCT

The polarization properties of the sample that is measured using PS-OCT can be fully described by a Jones matrix since the depolarization cannot be measured [15]. Here, we describe the general expression of the Jones matrix measurement using PS-OCT. In Fig. 1, the schematic diagram of a fiber-based PS-OCT is shown. To measure the Jones matrix of a sample, the states of polarization of the backscattered light with at least two incident states should be measured. The incident lights that have polarization states, $\mathbf{E}_{\text{in1}}, \mathbf{E}_{\text{in2}}$, pass through the system and are backscattered by the sample. The corresponding polarization states of the lights at the detector, $\mathbf{E}_{\text{out1}}, \mathbf{E}_{\text{out2}}$, can be expressed by using Jones calculus as follows:

$$\mathbf{E}_{\text{out1}}(z) = \begin{bmatrix} H_{\text{out1}}(z) \\ V_{\text{out1}}(z) \end{bmatrix} = \mathbf{J}(z)\mathbf{E}_{\text{out1}} = \mathbf{J}(z) \begin{bmatrix} H_{\text{in1}} \\ V_{\text{in1}} \end{bmatrix} \tag{1}$$

$$\mathbf{E}_{\text{out2}}(z) = \begin{bmatrix} H_{\text{out2}}(z) \\ V_{\text{out2}}(z) \end{bmatrix} = \mathbf{J}(z)\mathbf{E}_{\text{out2}}e^{i\psi} = \mathbf{J}(z) \begin{bmatrix} H_{\text{in2}} \\ V_{\text{in2}} \end{bmatrix} e^{i\psi} \tag{2}$$

where ψ is the phase difference between two incident lights. $\mathbf{J}$ is the Jones matrix of the system including the sample and optical fibers, and can be expressed as

$$\mathbf{J}(z) = \mathbf{J}_{\text{out}}\mathbf{J}_{\text{S,T}}(z)\mathbf{J}_{\text{in}}, \tag{3}$$

where $\mathbf{J}_{\text{S,T}}$ is the round-trip Jones matrix of the sample, and $\mathbf{J}_{\text{in}}, \mathbf{J}_{\text{out}}$ represent the Jones matrix of the optical fibers of the input and output paths. In general, the lights are divided into horizontal and vertical components by using polarizing optics, and interferometric signals at two orthogonal polarization states are detected. The detected interferometric signals can be expressed in the following matrix form:

$$\begin{bmatrix} \tilde{I}_{1,H}(z) & \tilde{I}_{2,H}(z) \\ \tilde{I}_{1,V}(z) & \tilde{I}_{2,V}(z) \end{bmatrix} = \begin{bmatrix} \eta_H H^*_{\text{ref}} & 0 \\ 0 & \eta_V V^*_{\text{ref}} \end{bmatrix} \mathbf{J}(z) \begin{bmatrix} H_{\text{in1}} & e^{i\psi}H_{\text{in2}} \\ V_{\text{in1}} & e^{i\psi}V_{\text{in2}} \end{bmatrix}, \tag{4}$$

#118929 - $15.00 USD Received 22 Oct 2009; revised 21 Dec 2009; accepted 23 Dec 2009; published 6 Jan 2010
(C) 2010 OSA

where $\tilde{I}_{i,p}$ (i = 1,2; p = H,V) is an OCT signal with i-th incident beam and p polarization detector; $H_{\text{ref}}, V_{\text{ref}}$, the electric field of the reference light on the horizontal and vertical channels of the detector, and η_H, η_V, the quantum efficiency of the horizontal and vertical channels. It is convenient to define the matrices of input electric fields and OCT signals as

$$\mathbf{E}_{\text{in}} = \begin{bmatrix} H_{\text{in1}} & H_{\text{in2}} \\ V_{\text{in1}} & V_{\text{in2}} \end{bmatrix} \tag{5}$$

$$\mathbf{S}(z) = \begin{bmatrix} \tilde{I}_{1,H}(z) & \tilde{I}_{2,H}(z) \\ \tilde{I}_{1,V}(z) & \tilde{I}_{2,V}(z) \end{bmatrix}. \tag{6}$$

Equation (4) can be rewritten as

$$\mathbf{S}(z) = \begin{bmatrix} \eta_H H_{\text{ref}}^* & 0 \\ 0 & \eta_V V_{\text{ref}}^* \end{bmatrix} \mathbf{J}(z) \mathbf{E}_{\text{in}} \begin{bmatrix} 1 & 0 \\ 0 & e^{i\Psi} \end{bmatrix}. \tag{7}$$

Thus, the Jones matrix $\mathbf{J}$ can be obtained by using the following formula:

$$\mathbf{J}(z) = \begin{bmatrix} \eta_H H_{\text{ref}}^* & 0 \\ 0 & \eta_V V_{\text{ref}}^* \end{bmatrix}^{-1} \mathbf{S}(z) \begin{bmatrix} 1 & 0 \\ 0 & e^{i\Psi} \end{bmatrix}^{-1} {\mathbf{E}_{\text{in}}}^{-1} \tag{8}$$

In previous single-mode fiber-based PS-OCT, the polarization states of light reflected at the reference point, e.g., the surface of the sample or a reflective material such as a glass plate in the sample arm, are used to cancel the effects of fiber components on the phase retardation measurement. It is achieved by multiplying the Jones matrix measured at the reference point with all other Jones matrices [16] in the following manner:

$$\begin{aligned} \mathbf{J}(z)\mathbf{J}(z_{\text{ref}})^{-1} &= \mathbf{J}_{\text{out}}\mathbf{J}_{\text{sample,T}}\mathbf{J}_{\text{out}}^{-1} \\ &= \begin{bmatrix} \eta_H H_{\text{ref}}^* & 0 \\ 0 & \eta_V V_{\text{ref}}^* \end{bmatrix}^{-1} \mathbf{S}(z)\mathbf{S}(z_{\text{ref}})^{-1} \begin{bmatrix} \eta_H H_{\text{ref}}^* & 0 \\ 0 & \eta_V V_{\text{ref}}^* \end{bmatrix}, \end{aligned} \tag{9}$$

where z_{ref} is the depth of the reference point, which is selected to be $\mathbf{J}(z_{\text{ref}}) = \mathbf{J}_{\text{out}}\mathbf{J}_{\text{in}}$.

Since $\mathbf{J}_{\text{S,T}}$ is transpose symmetric [17], $\mathbf{J}_{\text{S,T}}$ can be diagonalized by using an orthogonal matrix, i.e., a rotation matrix. This means that the two eigenvectors of $\mathbf{J}_{\text{S,T}}$ are orthogonal to each other. Hence, it can be decomposed with a linear retarder and a linear polarizer with the same optic axis [18].

By setting $\eta_H|H_{\text{ref}}| = \eta_V|V_{\text{ref}}|$ in an optical setup of PS-OCT, or by numerically compensating the reference amplitudes after the detection, the product of OCT signal matrices $\mathbf{M}(z_{\text{ref}}, z) = \mathbf{S}(z)\mathbf{S}(z_{\text{ref}})^{-1}$ can be expressed by using Eq. (9).

$$\mathbf{M}(z_{\text{ref}}, z) = \begin{bmatrix} 1 & 0 \\ 0 & e^{i\gamma} \end{bmatrix} \mathbf{J}_{\text{out}}\mathbf{J}_{\text{S,T}}\mathbf{J}_{\text{out}}^{-1} \begin{bmatrix} 1 & 0 \\ 0 & e^{i\gamma} \end{bmatrix}^{-1}, \tag{10}$$

where γ is the phase difference between the horizontal and vertical components of the reference light at the detector. This phase difference exists if the polarization state of the reference light at the detector is not linear. However, the value of γ is not required to obtain the phase retardation and diattenuation of the sample. Here the amplitude factor of reference beams is eliminated since it does not influence the following discussions. Since the matrix $[1,0;0,exp(i\gamma)]\mathbf{J}_{\text{out}}$ is unitary, the matrix $\mathbf{M}(z_{\text{ref}}, z)$ is unitarily similar to the sample Jones matrix $\mathbf{J}_{\text{S,T}}$. Hence, both the diagonalization method [16, 19] and methods assuming unitary transformed Jones matrix [18, 20] can be applied to obtain the sample phase retardation and diattenuation.

Note that knowledge of the exact polarization states of incident light is not required, and Eqs. (8) to (10) are valid unless two input polarization states are identical.

#118929 - $15.00 USD Received 22 Oct 2009; revised 21 Dec 2009; accepted 23 Dec 2009; published 6 Jan 2010
(C) 2010 OSA

2.2. *Local birefringence measurement*

The polarization properties of local tissues cannot be obtained from Eq. (10) since the Jones matrix includes polarization changes from the surface to a certain depth of the samples. Since in almost all single-mode fiber-based PS-OCTs, the reference point is set at the surface of a sample in order to neglect the influence of a fiber's birefringence, it is straightforward to shift the depth of the reference point adjacent to the depth of interest to avoid the birefringence of tissues above the interest point. To achieve the Jones matrix of the local tissue ranging from z_{i-n}–z_i, the signals of the backscattered lights at the depth of z_{i-n-1} are used as the reference. Equation (10) can then be rewritten as follows:

$$\mathbf{M}(z_{i-n-1},z_i)=\begin{bmatrix}1 & 0\\ 0 & e^{i\gamma}\end{bmatrix}\mathbf{J}_{\text{out}}\mathbf{J}_{\text{S,T}}(z_i)\left[\mathbf{J}_{\text{S,T}}(z_{i-n-1})\right]^{-1}\mathbf{J}_{\text{out}}^{-1}\begin{bmatrix}1 & 0\\ 0 & e^{i\gamma}\end{bmatrix}^{-1}. \tag{11}$$

The cumulative and round-trip sample Jones matrix $\mathbf{J}_{\text{S,T}}$ consists of single-trip Jones matrices of local sites as

$$\mathbf{J}_{\text{S,T}}(z_i)=\left[\mathbf{J}_{\text{S}}^{T}(z_1,z_2)\cdots\mathbf{J}_{\text{S}}^{T}(z_{i-1},z_i)\right]\left[\mathbf{J}_{\text{S}}(z_{i-1},z_i)\cdots\mathbf{J}_{\text{S}}(z_1,z_2)\right], \tag{12}$$

where $\mathbf{J}_{\text{S}}(z_i,z_{i+1})(i=1,2,3,\cdots)$ is the single-trip Jones matrix of the local tissue from the depth of z_i to z_{i+1}. Hence, Eq. (11) is rewritten as

$$\begin{aligned}\mathbf{M}(z_{i-n-1},z_i)=&\begin{bmatrix}1 & 0\\ 0 & e^{i\gamma}\end{bmatrix}\mathbf{J}_{\text{out}}\left[\mathbf{J}_{\text{S}}^{T}(z_1,z_2)\cdots\mathbf{J}_{\text{S}}^{T}(z_{i-n-2},z_{i-n-1})\right]\mathbf{J}_{\text{S,T}}(z_{i-n},z_i)\\ &\times\left[\mathbf{J}_{\text{S}}^{T}(z_1,z_2)\cdots\mathbf{J}_{\text{S}}^{T}(z_{i-n-2},z_{i-n-1})\right]^{-1}\mathbf{J}_{\text{out}}^{-1}\begin{bmatrix}1 & 0\\ 0 & e^{i\gamma}\end{bmatrix}^{-1}.\end{aligned} \tag{13}$$

where the Jones matrix $\mathbf{J}_{\text{S,T}}(z_{i-n},z_i)$ is the round-trip local polarization properties of the tissue located at the depth from z_{i-n} to z_i.

Since Eq. (13) is a similar matrix of $\mathbf{J}_{\text{S,T}}(z_{i-n},z_i)$, the eigenvalues of both matrices are identical [21]. The eigenvalues of the Jones matrix of the local tissue $\mathbf{J}_{\text{S,T}}(z_{i-n},z_i)$ will be obtained by the matrix diagonalization of $\mathbf{M}(z_{i-n-1},z_i)$. Equation (13) can be rewritten in a similarity transformation with the eigenvalues, $\lambda_{1,2}$, as

$$\mathbf{M}(z_{i-n-1},z_i)=\mathbf{A}\begin{bmatrix}\lambda_1 & 0\\ 0 & \lambda_2\end{bmatrix}\mathbf{A}^{-1}, \tag{14}$$

where

$$\lambda_{1,2} = \frac{\sqrt{R(z_i)}e^{i\phi(z_i)}}{\sqrt{R(z_{i-n})}e^{i\phi(z_{i-n})}}\exp\left[\pm\frac{\varepsilon(z_{i-n},z_i)+ir(z_{i-n},z_i)}{2}\right] \tag{15}$$

$$\mathbf{A} = \begin{bmatrix}1 & 0\\ 0 & e^{i\gamma}\end{bmatrix}\mathbf{J}_{\text{out}}\left[\mathbf{J}_{\text{S}}^{T}(z_1,z_2)\cdots\mathbf{J}_{\text{S}}^{T}(z_{i-n-2},z_{i-n-1})\right]\mathbf{R}(-\theta). \tag{16}$$

Here, $\lambda_{1,2}$ and $\mathbf{A}$ are the eigenvalues and eigenvector matrix of $\mathbf{M}(z_{i-n-1},z_i)$; $r(z_{i-n},z_i)$ and $\varepsilon(z_{i-n},z_i)$, the round-trip phase retardation and relative-attenuation [22], respectively, of the local tissue located at the depth from z_{i-n} to z_i; $\sqrt{R(z)}e^{i\phi(z)}$, a complex reflectivity coefficient at a depth of z; $\mathbf{R}(\theta)=[\cos(\theta),\sin(\theta);-\sin(\theta),\cos(\theta)]$, a rotation matrix where θ denotes the optic axis orientation of the local tissue. The local phase retardation and relative-attenuation can be calculated from the eigenvalues $\lambda_{1,2}$ as

$$r(z_{i-n},z_i) = \left|\tan^{-1}\frac{\text{Im}[\lambda_1/\lambda_2]}{\text{Re}[\lambda_1/\lambda_2]}\right| \tag{17}$$

$$\varepsilon(z_{i-n},z_i) = \ln|\lambda_1/\lambda_2|. \tag{18}$$

#118929 - $15.00 USD Received 22 Oct 2009; revised 21 Dec 2009; accepted 23 Dec 2009; published 6 Jan 2010
(C) 2010 OSA

Note that by using this method, local phase retardation and local relative-attenuation can be obtained even though diattenuation exists in the sample arm and tissues above the reference point (Appendix A). However, the relative optic axis orientation cannot be obtained from **A** if diattenuation exists.

If no diattenuation exists in the tissues and sample arm, the Jones matrices of local tissues and $\mathbf{J}_{\text{out}}$ are unitary. Hence, Eq. (13) becomes the unitary transform of the local Jones matrix $\mathbf{J}_{\text{S,T}}(z_{i-n}, z_i)$. The local phase retardation can be obtained by unitary transformation [16] or matrix trace [Eq. (38) in Ref. 18]:

$$r(z_{i-n}, z_i) = 2\cos^{-1}\frac{|\text{tr}\mathbf{M}|}{[2\text{tr}(\mathbf{M}^{\dagger}\mathbf{M})]^{1/2}}, \tag{19}$$

where the operators tr and det are the trace and determinant of a matrix, respectively. † indicates the complex conjugate transpose operation.

The local birefringence b of the tissue is calculated by

$$b(z_{i-n}, z_i) = \frac{r(z_{i-n}, z_i)}{2k_0\Delta z}, \tag{20}$$

where k_0 is the center wavenumber of the light source in space, and $\Delta z = z_i - z_{i-n}$ is the thickness of the measured local tissue. The factor 2 is a result of the round-trip propagation in the sample. The large separation Δz gives us a large local phase retardation. Consequently, a high contrast in local birefringence imaging is obtained. However, the axial resolution is reduces.

3. Noise performance of generalized Jones matrix OCT

The signal-to-noise ratio of OCT signals might have significant roles in the performance of the phase retardation measurement. The systematic error in amplitude-based PS-OCT [5] due to background noise has already been reported [23, 24]. However, the error in the Jones matrix method has not been investigated yet. In this section, the systematic phase retardation error due to additive background noise is theoretically described and compared with numerical simulations and experimental results. The performance of the phase retardation measurement depending on the signal-to-noise ratio is then discussed.

3.1. Analysis methods

3.1.1. Theoretical analysis of the matrix trace method

In order to mathematically describe the tendency of the systematic error in phase retardation, the error propagation analysis is applied from the detected OCT signals [Eq. (6)] to the product of OCT signal matrices **M**, and the measured phase retardation with background noise is obtained. Signal matrices with background noises can be defined as

$$\mathbf{S} = \mathbf{S}_0 + \begin{bmatrix} \Delta Ir_{11} + i\Delta Ii_{11} & \Delta Ir_{12} + i\Delta Ii_{12} \\ \Delta Ir_{21} + i\Delta Ii_{21} & \Delta Ir_{22} + i\Delta Ii_{22} \end{bmatrix} \tag{21}$$

$$\mathbf{S}' = \mathbf{S}'_0 + \begin{bmatrix} \Delta Ir'_{11} + i\Delta Ii'_{11} & \Delta Ir'_{12} + i\Delta Ii'_{12} \\ \Delta Ir'_{21} + i\Delta Ii'_{21} & \Delta Ir'_{22} + i\Delta Ii'_{22} \end{bmatrix}, \tag{22}$$

where **S** and **S**′ are the measured signal matrices for measurement and reference, respectively. ΔIr_{ij} and ΔIi_{ij} are the errors of the real and imaginary parts due to background noises, respectively. The errors in the matrix **M** are defined as

$$\mathbf{M} = \mathbf{M}_0 + \begin{bmatrix} \Delta Mr_{11} + i\Delta Mi_{11} & \Delta Mr_{12} + i\Delta Mi_{12} \\ \Delta Mr_{21} + i\Delta Mi_{21} & \Delta Mr_{22} + i\Delta Mi_{22} \end{bmatrix}, \tag{23}$$

#118929 - $15.00 USD Received 22 Oct 2009; revised 21 Dec 2009; accepted 23 Dec 2009; published 6 Jan 2010
(C) 2010 OSA

where

$$\begin{aligned}\mathbf{M}_0 &= \mathbf{S}_0\,\mathbf{S'}_0^{-1} \\ &= \begin{bmatrix}\tilde{I}_{1,H} & \tilde{I}_{2,H}\\ \tilde{I}_{1,V} & \tilde{I}_{2,V}\end{bmatrix}\begin{bmatrix}\tilde{I'}_{1,H} & \tilde{I'}_{2,H}\\ \tilde{I'}_{1,V} & \tilde{I'}_{2,V}\end{bmatrix}^{-1}.\end{aligned} \tag{24}$$

In order to obtain the errors in the product matrix in Eq. (23), the error propagation analysis is applied as

$$\Delta Mr_{11} = \Delta Mi_{11} = \frac{\sqrt{|\tilde{I}'_{2,V}|^2\Delta I_{11}^2 + |\tilde{I}'_{1,V}|^2\Delta I_{12}^2 + |\tilde{I}_{2,H}|^2\Delta I'^2_{21} + |\tilde{I}_{1,H}|^2\Delta I'^2_{22}}}{|\det \mathbf{S}'_0|} \tag{25}$$

$$\Delta Mr_{12} = \Delta Mi_{12} = \frac{\sqrt{|\tilde{I}'_{2,H}|^2\Delta I_{11}^2 + |\tilde{I}_{2,H}|^2\Delta I'^2_{11} + |\tilde{I}'_{1,H}|^2\Delta I_{12}^2 + |\tilde{I}_{1,H}|^2\Delta I'^2_{21}}}{|\det \mathbf{S}'_0|} \tag{26}$$

$$\Delta Mr_{21} = \Delta Mi_{21} = \frac{\sqrt{|\tilde{I}'_{2,V}|^2\Delta I_{21}^2 + |\tilde{I}_{2,V}|^2\Delta I'^2_{21} + |\tilde{I}'_{1,V}|^2\Delta I_{22}^2 + |\tilde{I}_{1,V}|^2\Delta I'^2_{22}}}{|\det \mathbf{S}'_0|} \tag{27}$$

$$\Delta Mr_{22} = \Delta Mi_{22} = \frac{\sqrt{|\tilde{I}_{2,V}|^2\Delta I'^2_{11} + |\tilde{I}_{1,V}|^2\Delta I'^2_{21} + |\tilde{I}'_{2,H}|^2\Delta I_{21}^2 + |\tilde{I}'_{1,V}|^2\Delta I_{22}^2}}{|\det \mathbf{S}'_0|}. \tag{28}$$

Here it is assumed that the errors in the interference signals are independent of each other; however, the fluctuations in the real and imaginary parts of each interference signal have the same magnitude, $\Delta I_{ij} = \Delta Ir_{ij} = \Delta Ii_{ij}$. This assumption of the inter-independency of the noise is valid as far as the OCT system operates in the shot-noise-limited or detector-noise-limited regimes. From Eqs. (23) to (28), the magnitudes of the denominator and numerator of Eq. (19) are obtained. The phase retardation with background noise can be expressed as

$$r_m = 2\cos^{-1}\left[\frac{\sqrt{2\mathrm{tr}[\mathbf{M}_0^\dagger\mathbf{M}_0]\cos^2\frac{r}{2} + \frac{2\Delta I^2}{|\det \mathbf{S}'_0|^2}(\mathrm{tr}[\mathbf{S}_0^\dagger\mathbf{S}_0] + \mathrm{tr}[\mathbf{S'}_0^\dagger\mathbf{S}'_0])}}{\sqrt{2}\sqrt{\mathrm{tr}[\mathbf{M}_0^\dagger\mathbf{M}_0] + \frac{4\Delta I^2}{|\det \mathbf{S}'_0|^2}(\mathrm{tr}[\mathbf{S}_0^\dagger\mathbf{S}_0] + \mathrm{tr}[\mathbf{S'}_0^\dagger\mathbf{S}'_0])}}\right]. \tag{29}$$

Here we have assumed that all the errors in each component of the matrix $\mathbf{M}$ [Eqs. (25) to (28)] are independent of each other; moreover, among the real and imaginary parts, and the noise power of each channel are identical, i.e., $2\Delta I^2 = 2\Delta I_{11}^2 = 2\Delta I_{12}^2 = 2\Delta I_{21}^2 = 2\Delta I_{22}^2$. In reality, some noise components are not independent to each other; some components share original raw signals. For more accurate analysis, rigorous treatments of statistical properties of these components are required. Neglecting the correlations among noise components will cause perturbation in results. However, it is not large and major tendency is preserved as shown in Sec. 3.3.

In Eq. (19), we have assumed the absence of diattenuation of the sample. By using this assumption in Eq. (29), this equation can be further simplified. Because of the absence of diattenuation, the measured Jones matrix $\mathbf{J}$ is considered as a unitary matrix and can be expressed as follows:

$$\mathbf{J} = \sqrt{R}\begin{bmatrix}a & -b^*\\ b & a^*\end{bmatrix}, \tag{30}$$

where R is the intensity reflection coefficient and $|a|^2 + |b|^2 = 1$. Consequently, the signal matrix will be described using Eq. (4) as

$$\mathbf{S} = \eta\sqrt{RI_{\mathrm{ref}}}\begin{bmatrix}aH_{\mathrm{in1}} - b^*V_{\mathrm{in1}} & aH_{\mathrm{in2}} - b^*V_{\mathrm{in2}}e^{i\psi}\\ bH_{\mathrm{in1}} + a^*V_{\mathrm{in1}}e^{i\gamma} & bH_{\mathrm{in2}} + a^*V_{\mathrm{in2}}e^{i\gamma}e^{i\psi}\end{bmatrix}. \tag{31}$$

#118929 - $15.00 USD Received 22 Oct 2009; revised 21 Dec 2009; accepted 23 Dec 2009; published 6 Jan 2010
(C) 2010 OSA

Here, it is assumed that the signal efficiency of both horizontal and vertical channels are balanced, i.e., $\eta_H|H_{\text{ref}}| = \eta_V|V_{\text{ref}}| = \eta\sqrt{I_{\text{ref}}}$. The absolute of the determinant of Eq. (31) becomes

$$|\det \mathbf{S}| = \eta^2 R I_{\text{ref}} |\det \mathbf{E}_{\text{in}}|. \tag{32}$$

We found that $|\det \mathbf{E}_{\text{in}}|$ is the absolute of the inner product between the two Jones vectors $[H_{\text{in1}}, V_{\text{in1}}]^T$ and $[V_{\text{in2}}, -H_{\text{in2}}]^T$; these represent two incident polarization states, but one is rotated to become orthogonal to the original $[V_{\text{in2}}, -H_{\text{in2}}]^T \perp [H_{\text{in2}}, V_{\text{in2}}]^T$. Hence, the absolute determinant can be expressed using an angle ζ between two Stokes vectors, which corresponds to the two input polarization states on Poincaré sphere as

$$|\det \mathbf{E}_{\text{in}}| = |H_{\text{in1}}V_{\text{in2}} - V_{\text{in1}}H_{\text{in2}}| = \sqrt{I_{\text{in1}}I_{\text{in2}}}|\sin\zeta/2|, \tag{33}$$

where $I_{\text{in1}} = |H_{\text{in1}}|^2 + |V_{\text{in1}}|^2$ and $I_{\text{in2}} = |H_{\text{in2}}|^2 + |V_{\text{in2}}|^2$ are the intensities of two incident lights.

According to Eqs. (31)–(33), each term of Eq. (29) becomes the following:

$$\begin{aligned}
\text{tr}[\mathbf{S}_0^\dagger \mathbf{S}_0] &= \eta^2 R I_{\text{ref}}(I_{\text{in1}} + I_{\text{in2}}) && (34)\\
|\det \mathbf{S'}_0| &= \eta^2 R' I_{\text{ref}} \sqrt{I_{\text{in1}}I_{\text{in2}}}|\sin\zeta/2| && (35)\\
\text{tr}[\mathbf{M}_0^\dagger \mathbf{M}_0] &= 2\frac{R}{R'} && (36)\\
& && (37)
\end{aligned}$$

By substituting Eqs. (34–36) into Eq. (29), the measured phase retardation with background noise can be described as

$$r_m = 2\cos^{-1}\left[\frac{\sqrt{\cos^2\frac{r}{2} + ESNR_{PR}^{-1}\csc^2\frac{\zeta}{2}}}{\sqrt{1 + 4ESNR_{PR}^{-1}\csc^2\frac{\zeta}{2}}}\right]. \tag{38}$$

where $ESNR_{PR}$ is the effective SNR of the phase retardation measurement; it is defined as

$$\frac{1}{ESNR_{PR}} = \frac{1}{4}\left(\frac{1}{SNR_1} + \frac{1}{SNR_2} + \frac{1}{SNR'_1} + \frac{1}{SNR'_2}\right). \tag{39}$$

$SNR_k (k = 1, 2)$ is the signal-to-noise ratio of an OCT signal with a k-th input light. Then, $SNR_k = \eta^2 R I_{\text{ref}} I_{\text{ink}}/(2\Delta I^2)$.

3.1.2. Numerical simulations

Numerical simulations of phase retardation measurements with background noise are performed in order to investigate the error and statistical properties for both matrix trace and diagonalization methods. For simulations, the Monte-Carlo method is used. The measured signals are assumed to have additive complex noises as follows:

$$\begin{bmatrix} \tilde{I}_{1,H}(z) & \tilde{I}_{2,H}(z) \\ \tilde{I}_{1,V}(z) & \tilde{I}_{2,V}(z) \end{bmatrix} = \mathbf{J}\begin{bmatrix} H_{\text{in1}} & H_{\text{in2}} \\ V_{\text{in1}} & V_{\text{in2}} \end{bmatrix} + \begin{bmatrix} \mathbf{n}_{11}(z) & \mathbf{n}_{12}(z) \\ \mathbf{n}_{21}(z) & \mathbf{n}_{22}(z) \end{bmatrix}, \tag{40}$$

where $\mathbf{n}_{lm}$ obeys complex normal distributions in which the real and imaginary parts are independent Gaussian variables and have zero-mean and identical standard deviation σ_{lm}. Eight normal random variables are numerically generated and added to theoretical signals. Their standard deviations are defined by parameters SNR_m as $2\sigma_{lm}^2 = (|H_{\text{inm}}|^2 + |V_{\text{inm}}|^2)/SNR_m$.

The models of two Jones matrices are defined as follows. The reference Jones matrix is constructed with the following two arbitrary unitary matrices:

$$\mathbf{J}' = \mathbf{J}_{U1}\mathbf{J}_{U2}. \tag{41}$$

#118929 - $15.00 USD Received 22 Oct 2009; revised 21 Dec 2009; accepted 23 Dec 2009; published 6 Jan 2010
(C) 2010 OSA

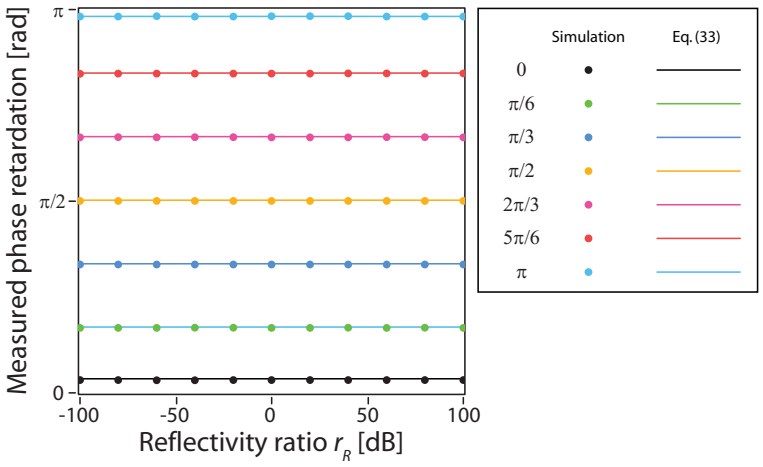

Fig. 2. The relationship between phase retardation and the ratio of SNRs. $ESNR_{PR}$ = 30 dB and incident intensity ratio r_I = 1.

$\mathbf{J}_U$ is the unitary matrix that has the determinant of unity. The Jones matrix measured at below the target is then

$$\mathbf{J} = \mathbf{J}_{U1}\mathbf{J}_{lr}(r,\theta)\mathbf{J}_{U2}, \tag{42}$$

where $\mathbf{J}_{lr}(r,\theta)$ is the Jones matrix of a linear retarder with retardation r and its optic axis orientation θ.

Two matrices of eight numerically generated OCT signals are processed using matrix diagonalization and the matrix trace method [Eq. (19)]. It is applied for several trials, and the distribution of resulting phase retardations can be obtained.

3.1.3. Experiment

In order to compare the theoretical phase retardation error and simulation results with experimental results, measurements using a glass plate were performed. In this experiment, we utilized a swept-source PS-OCT system with continuous polarization modulation [25]. In this system, the input light is modulated by a polarization modulator. It can be considered that there are two orthogonal incident polarization states wherein the phase of one of the states is modulated. This configuration provides the following conditions. $ESNR_{PR}^{-1}(z_{i-n},z_i) = \left(1+\frac{1}{J_1^2(A0)}\right)(SNR_1(z_i)^{-1}+SNR_1(z_{i-n})^{-1})/4$, and $\sin^2\zeta/2 = 1$.

The glass plate at the sample arm is measured using the PS-OCT with a variable attenuator. A sequence of 1000 axial profiles is acquired. Another set of data with a different SNR is then obtained by changing the attenuation. The phase retardations of each data set are calculated using signals at the front and back surfaces of the glass plate. $ESNR_{PR}$ is calculated according to Eq. (39). It is assumed that the glass plate has no birefringence, i.e., it will provide zero phase retardation. The measured OCT signals are processed by the diagonalization and matrix trace methods [Eq. (19)].

3.2. Validity of $ESNR_{PR}$

The theoretical analysis (Sec. 3.1.1) shows that the phase retardation error depends on $ESNR_{PR}$, which is a linear combination of four inverted SNRs with two incident polarization states and two different targets [Eq. (39)]. To validate that the measured retardation depends only on this

#118929 - $15.00 USD Received 22 Oct 2009; revised 21 Dec 2009; accepted 23 Dec 2009; published 6 Jan 2010
(C) 2010 OSA

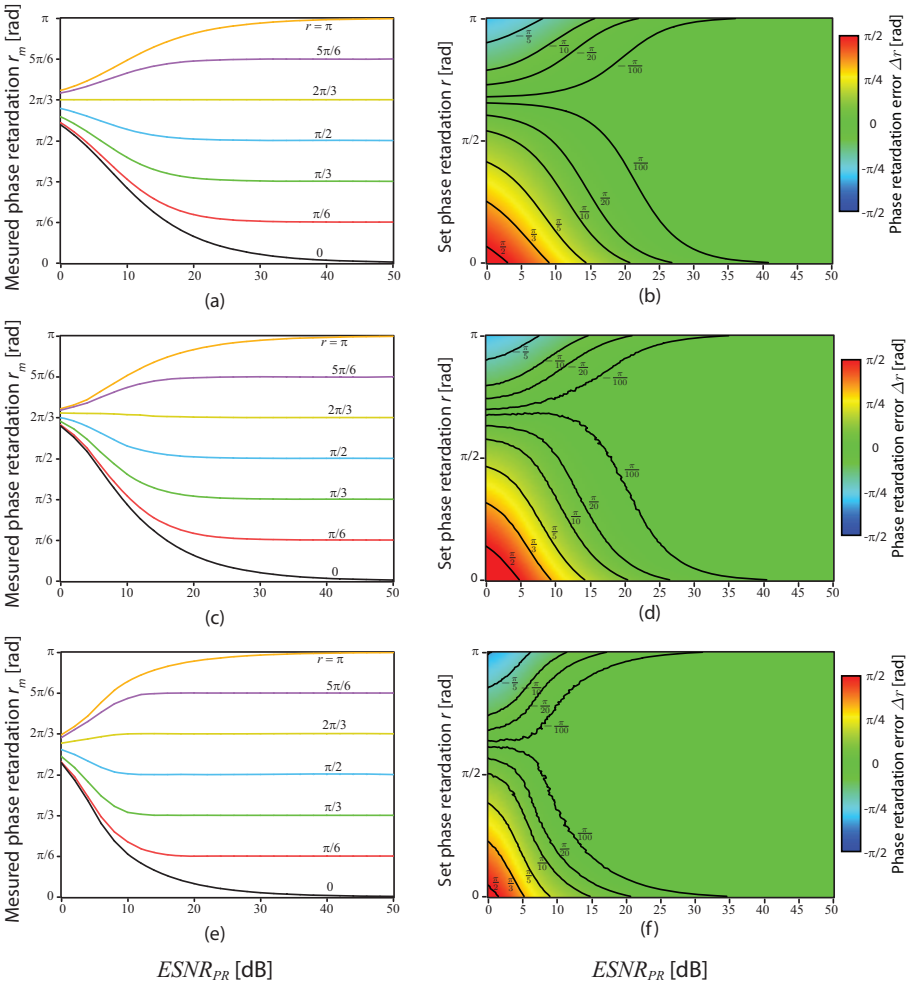

Fig. 3. (a, c, e) Measured phase retardations with several set phase retardations r and (b, d, f) contour plots of phase retardation error $\Delta r = r - r_m$ obtained by theoretical analysis according to Eq. (38) (a, b), Monte Carlo simulations of matrix trace method by using Eq. (19) (c, d), and diagonalization method (e, f).

$ESNR_{PR}$, numerical simulations have been performed with different ratios between SNRs while the $ESNR_{PR}$ values are identical. It is defined that $1/ESNR_{PR} = (1+r_R)(1+r_I)/(4SNR_1)$, where $r_R = R/R_{\text{ref}}$ and $r_I = I_{\text{in1}}/I_{\text{in2}}$. The numerical simulation results and the theoretical curve of Eq. (19) are shown in Fig. 2. The phase retardation does not depending on the ratio of the SNRs. Hence, $ESNR_{PR}$ is effective to evaluate the performance of the phase retardation measurement.

3.3. Error in phase retardation measurement

The estimated measured phase retardations at several set phase retardations are plotted as shown in Figs. 3(a), 3(c), and 3(e). In the Monte Carlo simulation results, the phase retardation is obtained by averaging 16384 trials. It is clear that the measured phase retardation erroneously approaches around $\frac{2\pi}{3}$ rad as $ESNR_{PR}$ decreases. The phase retardation error $\Delta r = r - r_m$ is

#118929 - $15.00 USD Received 22 Oct 2009; revised 21 Dec 2009; accepted 23 Dec 2009; published 6 Jan 2010
(C) 2010 OSA

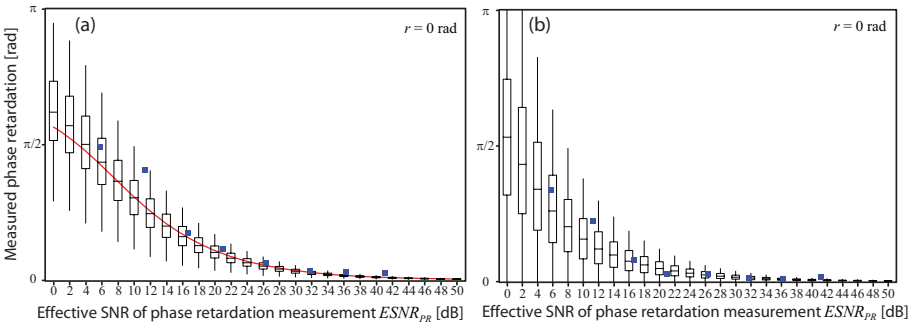

Fig. 4. Plots of phase retardation with background error in (a) matrix trace method and (b) diagonalization method, where the set phase retardation r = 0 radian. The red curve shows the result of theoretical analysis. The box and whisker plots exhibit the distribution from the simulation. Blue squares are the experimental results. The retardation of the local tissue is set to zero.

mapped on Figs. 3(b), 3(d), 3(f). It shows that phase retardation error increases as $ESNR_{PR}$ decreases. These results are identical to those from the amplitude-based PS-OCT method [23], except the asymptotic value of phase retardation at lower SNR. It is $\frac{\pi}{2}$ rad (double pass) for the amplitude-based PS-OCT [23]. The diagonalization method exhibits a smaller retardation error than the matrix trace method, and the distribution of the retardation error is closer to the symmetric.

The theoretical curve, simulated values, and experimental values of the measured phase retardation are plotted in Fig. 4. Figure 4(a) shows the results based on the trace method. The experimental results (blue rectangles) are in good agreement with both the theoretical analysis results calculated by Eq. (38) (red curve) and the numerical simulation results (box and whisker plots). The results show that the phase retardation error due to background noise strongly depends on $ESNR_{PR}$. Since $ESNR_{PR}$ is dominated by the lowest SNR of its constituents, the retardation error strongly depends on the lowest SNR of the four detection channels. The experimental results (blue rectangles) and numerical simulations (box and whisker plots) using the diagonalization method are also in good agreement, as shown in Fig. 4(b). The diagonalization method exhibits a smaller discrepancy between the ideal retardation and resulting retardation at low $ESNR_{PR}$ values.

The difference in the methods is perhaps a result of the characterization of diattenuation. The random noises may be accounted as pseudo-diattenuation. Since in the diagonalization method, sample diattenuation does not produce phase retardation error (Appendix A), the retardation error is suppressed. Alternatively, random noises will affect eigenvectors. Although the phase retardation error is small, the distribution is spread more widely than the results of the matrix trace method at very low $ESNR_{PR}$ values.

Figures 5 and 6 show the distribution of the phase retardation obtained by numerical simulations and experiments both in the case of the diagonalization method (Fig. 5) and matrix trace method (Fig. 6), where the set phase retardation is 0 radian. They show that the distributions for both the simulation and experimental results are in good agreement. As $ESNR_{PR}$ decrease, the distribution is distorted and becomes asymmetrical. Although $ESNR_{PR}$ is high [Figs. 5(e), 5(f), 6(e), 6(f)], the discrepancies from the set phase retardation are significant since the value is close to the edge of the phase retardation range $[0,\pi)$ [7]. It is hence suggested that a simple averaging of the phase retardation is not a proper estimator.

#118929 - $15.00 USD Received 22 Oct 2009; revised 21 Dec 2009; accepted 23 Dec 2009; published 6 Jan 2010
(C) 2010 OSA

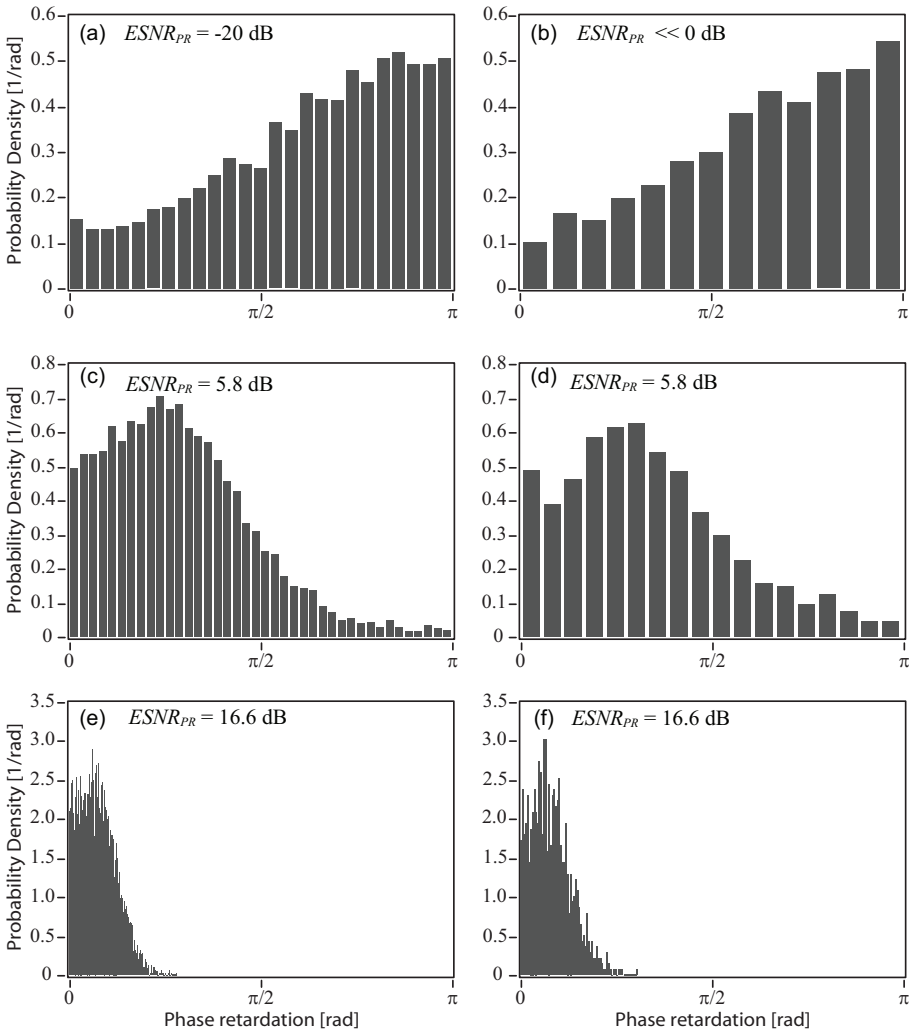

Fig. 5. Comparison of the histograms obtained by numerical simulations and experiments by using the diagonalization method. There is no phase retardation in the sample. (a),(c),(e) are the results of numerical simulations and (b),(d),(f) are the experimental results. $ESNR_{PR}$ was set to be -20, 5.8, and 16,6 dB from the top row for the simulations. The measured $ESNR_{PR}$ in experiments were 5.8 and 16.6 dB for (d) and (f). There is no light illuminated on the glass plate for (b).

#118929 - $15.00 USD Received 22 Oct 2009; revised 21 Dec 2009; accepted 23 Dec 2009; published 6 Jan 2010
(C) 2010 OSA

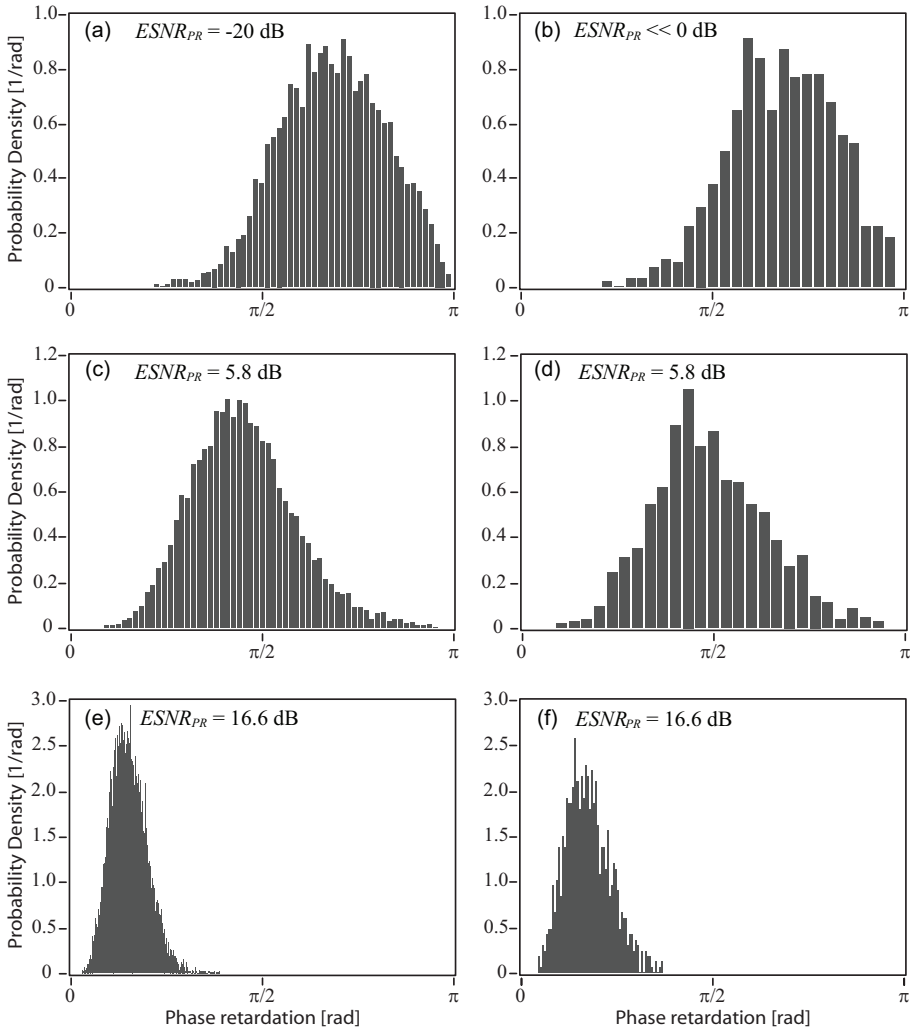

Fig. 6. Comparison of the histograms obtained by numerical simulation and experiment by using the matrix trace method. There is no phase retardation in the sample. (a),(c),(e) are the results of numerical simulation and (b),(d),(f) are the experimental results. The $ESNR_{PR}$ was set to be -20, 5.8, and 16,6 dB from the top row for simulation. The measured $ESNR_{PR}$ in the experiments are 5.8 and 16.6 dB for (d) and (f), respectively. There is no light illuminated on the glass plate for (b).

#118929 - $15.00 USD Received 22 Oct 2009; revised 21 Dec 2009; accepted 23 Dec 2009; published 6 Jan 2010
(C) 2010 OSA

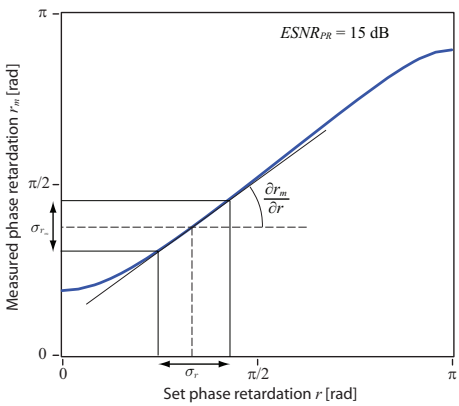

Fig. 7. Relationship between set phase retardation and measured phase retardation. The standard deviation of phase retardation σ_{r_m} is distorted due to the nonlinear relationship between the set phase retardation and measured phase retardation.

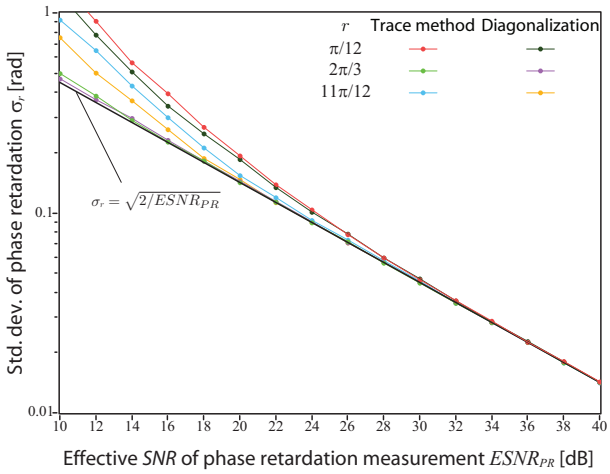

Fig. 8. Log-log plots of standard deviation of phase retardation to $ESNR_{PR}$. In both methods, the standard deviations are approaching to $\sigma_r = \sqrt{2/ESNR_{PR}}$ as $ESNR_{PR}$ increases. The diagonalization method exhibits slightly lower standard deviation than that of the trace method at low $ESNR_{PR}$.

3.4. Accuracy of phase retardation measurements.

Fluctuations of measured phase retardation limit the accuracy of the measurement. In the previous section, we found that the background noises resulted in either systematic overestimation or underestimation of phase retardation, not only in the fluctuation of the measured phase retardation. The fluctuations in the measured phase retardation do not represent the accuracy directly. Figure 7 illustrates an example of the relationship between set and measured retardations. The standard deviation in phase retardation with respect to the set retardation can be defined using the slopes of the set and measured retardation curves as

$$\sigma_r = \frac{\sigma_{r_m}}{\frac{\partial r_m}{\partial r}}, \tag{43}$$

#118929 - $15.00 USD Received 22 Oct 2009; revised 21 Dec 2009; accepted 23 Dec 2009; published 6 Jan 2010
(C) 2010 OSA

where σ_{r_m} is the standard deviation of the measured phase retardation and $\partial r_m/\partial r$ is the slope of the curve. The derivatives are calculated by using the differences between the mean of the measured phase retardation.

In Fig. 8, the standard deviations of phase retardation are plotted against $ESNR_{PR}$. Near the edge of the phase retardation measurement range ($r = \pi/12, 11\pi/12$), the standard deviation in the diagonalization method is smaller than that in the matrix trace method. It seems that there is a linear relationship between $\log\sigma_r$ and $\log ESNR_{PR}$, particularly in the case of the $2\pi/3$ set retardation, which exhibits a low phase retardation error (Fig. 3).

Since the phase retardation is the phase difference between the complex eigenvalues of the sample Jones matrix [Eq. (14)], it is expected that the relationship between the standard deviation of phase retardation and $ESNR_{PR}$ will be similar to that between the phase difference and SNR of complex signals; $\sigma_{\Delta\phi} = \sqrt{1/SNR}$ [26, 27]. In addition, the optic axis determination accuracy of the Stokes-vector method also exhibits a similar tendency [28]. A line fitting to the curves of the $2\pi/3$ set phase retardation at high $ESNR_{PR}$ values ($>$ 10 dB) has been applied using the regression model $\log\sigma_r = 1/2(\log a - \log ESNR_{PR})$, which is equivalent to $\sigma_r = \sqrt{a/ESNR_{PR}}$. The fitting to both the simulation results with the matrix trace and diagonalization methods reveals a fitting coefficient $a = 2.0$. Figure 8(b) shows that all the curves approach the line of $\sigma_r = \sqrt{2/ESNR_{PR}}$ at high $ESNR_{PR}$ values. This is probably a fundamental limit of the phase retardation measurement with additive noise at large $ESNR_{PR}$.

4. Local birefringence imaging

The local birefringence algorithm is applied for the PS-OCT images of biological tissues. The human anterior eye chamber and skin are measured using a 1.3–μm swept-source PS-OCT [25]. An informed consent was obtained from all subjects. All protocols adhered to the tenets of the Declaration of Helsinki and were approved by the Institutional Review Board of the University of Tsukuba. The scanning rate of the wavelength-swept light source is 20 kHz, and its tuning band width is 110 nm. An axial resolution of 11.9 μ is provided in the tissue.

The phase retardation imaging of the anterior eye chamber is a promising application. For quantitatively evaluating the risk of angle-closure glaucoma by using OCT, the detection of landmark structures such as trabecular meshwork is important. Figure 9 shows a comparison of the OCT, cumulative phase retardation, and local birefringence images, which have been prepared from a data set of subject 6 in Ref. 29. The axial separation of two measurement points is approximately 77.3 μm in the tissue. The phase retardation and local birefringence images are smoothed by a median filter with a 3×3 cross-shaped neighborhoods. The local birefringence images exhibit a high birefringent tissue near the angle. This might correspond to the trabecular meshwork, which is a drainage channel of aqueous humor. A layer with a relatively high birefringence appeared in the sclera. Collagen bundles in the sclera may account for this high birefringence. The local birefringence image obtained by using diagonalization [Fig. 9(c)] exhibits a better contrast than that obtained by using the matrix trace method in which the sample diattenuation is ignored [Fig. 9(d)]. Figure 9(d) exhibits artificial birefringence in the tissues anterior to the sclera and iris, although they might have no birefringence. The diagonalization method exhibits a better contrast in the local birefringence imaging.

Cross-sectional OCT, phase retardation, and local birefringence images of the human skin are shown in Fig. 10. The axial distance between two measurement points for local birefringence calculations is 67.1 μm. Phase retardation and local birefringence images are smoothed by a median filter with a 3×3 cross-shaped neighborhoods. An inhomogeneous distribution of birefringent tissues is shown. The distribution of the local birefringence appears more clearly in *en-face* slices (Fig. 11). Speckle-like noises in *en-face* slices are removed by a median filter with a 3×3 cross-shaped neighborhoods. A high birefringence appears around the dark

#118929 - $15.00 USD Received 22 Oct 2009; revised 21 Dec 2009; accepted 23 Dec 2009; published 6 Jan 2010
(C) 2010 OSA

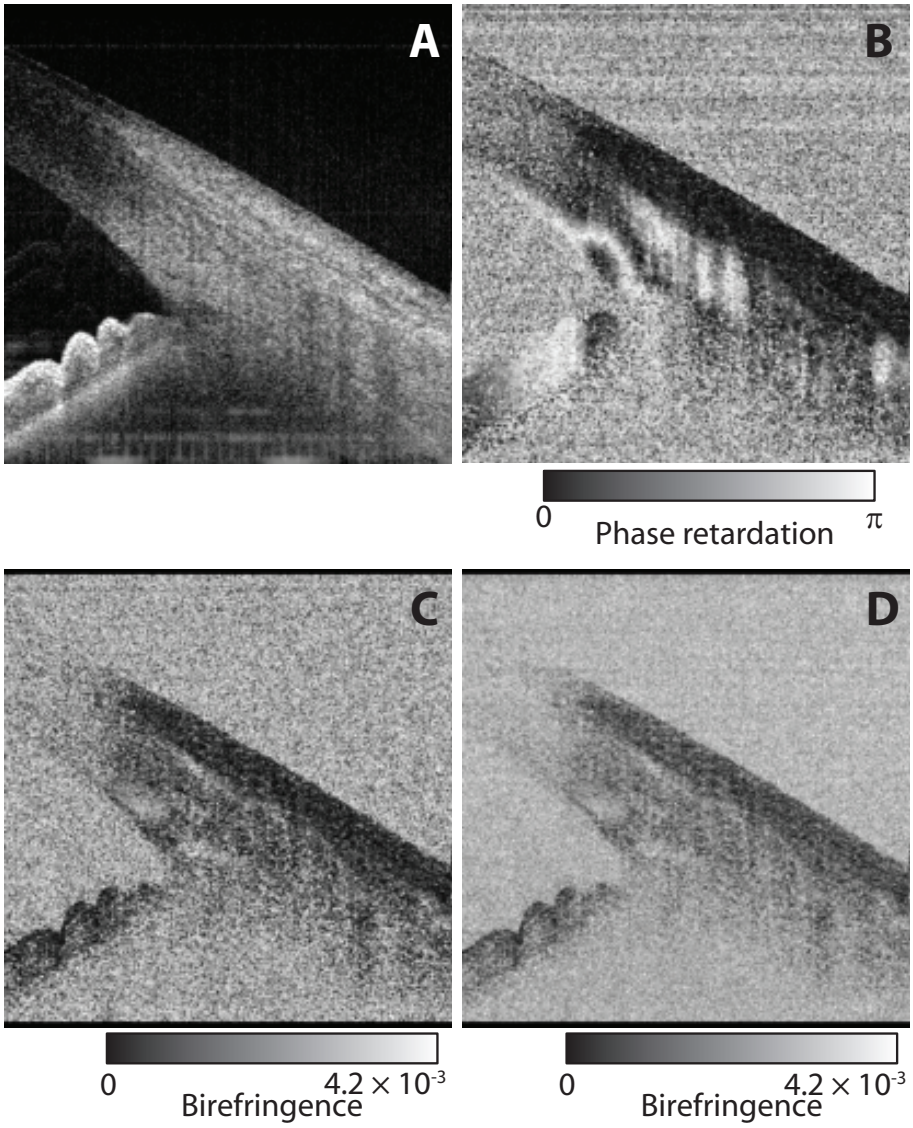

Fig. 9. Cross-sectional PS-OCT images of the human anterior eye chamber *in vivo*. (A) polarization-insensitive OCT image; (B) conventional cumulative phase retardation image; (C) local birefringence image with diagonalization method; and (D) local birefringence image using matrix trace method.

#118929 - $15.00 USD Received 22 Oct 2009; revised 21 Dec 2009; accepted 23 Dec 2009; published 6 Jan 2010
(C) 2010 OSA

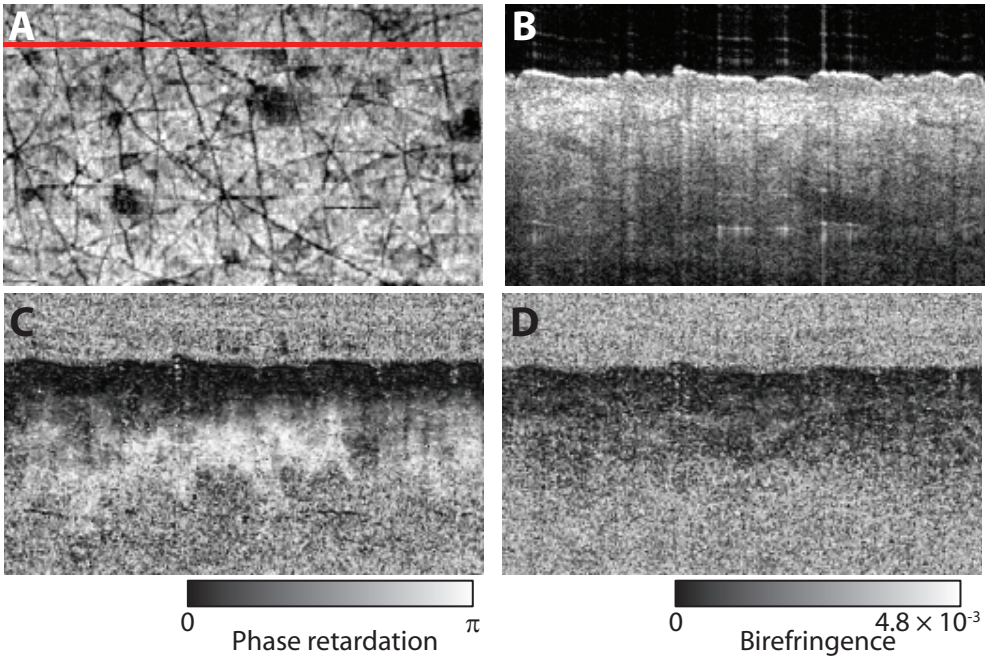

Fig. 10. Cross-sectional images of the human skin. (A) The *en-face* projection image indicates the location of cross sections; (B) Polarization-insensitive OCT image; (C) cumulative phase retardation image; (D) local retardation image by using diagonalization method.

spots in the dermis, as shown in Figs. 11(f) and 11(g). They may corresponding to highly dense collagenous fiber bundles around the infundibulum [30]. The averaged birefringence at this high birefringent tissue [Fig. 11(f), yellow box] is 1.96 $\times 10^{-3}$. This is in good agreement with birefringence of collagen measured ($1.59 \times 10^{-3} \sim 3.0 \times 10^{-3}$) [31].

The local birefringence imaging exhibits a better discrimination of birefringent tissues, which had been difficult to achieve previously in conventional cumulative phase retardation imaging [32]. In cumulative phase retardation OCT images, the existence of birefringence appears as changes in the phase retardation along the depth [29, 33]. The local birefringence imaging will provide more intuitive birefringent tissue discrimination.

5. Discussion

5.1. Boundary effect on local birefringence imaging

The boundary effect will occur when the region of interest (ROI) of the local phase retardation measurement covers the boundary between the tissues with different birefringences. Figure 12 shows the schematic diagram of the ROI in the sample with two tissues. It can be modeled with Jones matrices, and local birefringence measurement will be simulated.

Single-trip Jones matrices of two tissues can be expressed as

$$\mathbf{J}_1(z_u, z_d) = \mathbf{R}(-\theta_1) \begin{bmatrix} \exp[i\int_{z_u}^{z_d} \frac{b_1}{2} kzdz] & 0 \\ 0 & \exp[-i\int_{z_u}^{z_d} \frac{b_1}{2} kzdz] \end{bmatrix} \mathbf{R}(\theta_1) \quad (44)$$

$$\mathbf{J}_2(z_u, z_d) = \mathbf{R}(-\theta_2) \begin{bmatrix} \exp[i\int_{z_u}^{z_d} \frac{b_2}{2} kzdz] & 0 \\ 0 & \exp[-i\int_{z_u}^{z_d} \frac{b_2}{2} kzdz] \end{bmatrix} \mathbf{R}(\theta_2), \quad (45)$$

#118929 - $15.00 USD Received 22 Oct 2009; revised 21 Dec 2009; accepted 23 Dec 2009; published 6 Jan 2010
(C) 2010 OSA

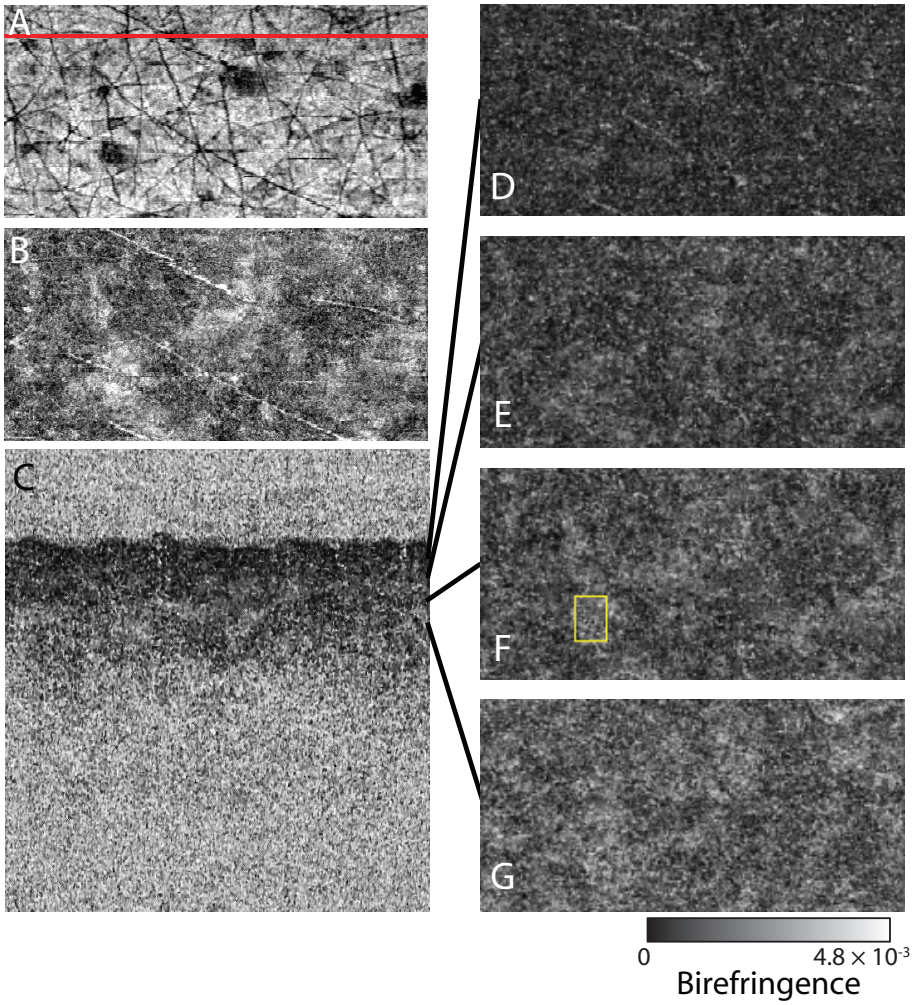

Fig. 11. *En-face* local birefringence images of the human skin. The projections of (A) polarization-insensitive OCT and (B) local birefringence images show the distribution of pores and high birefringence around them. *En-face* local birefringence images at the depths of (D) 144; (E) 211; (F) 267; and (G) 383 μm are shown. (C) cross-sectional local retardation image by using diagonalization method. An averaged birefringence inside the yellow box in (F) is 1.96 $\times 10^{-3}$.

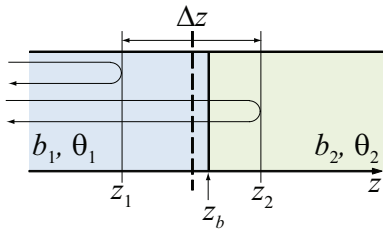

Fig. 12. Schematic diagram of the tissue boundary. Tissues 1 and 2 have the birefringences b_1 and b_2, respectively. Their optic axis orientations are θ_1 and θ_2, respectively.

#118929 - $15.00 USD Received 22 Oct 2009; revised 21 Dec 2009; accepted 23 Dec 2009; published 6 Jan 2010
(C) 2010 OSA

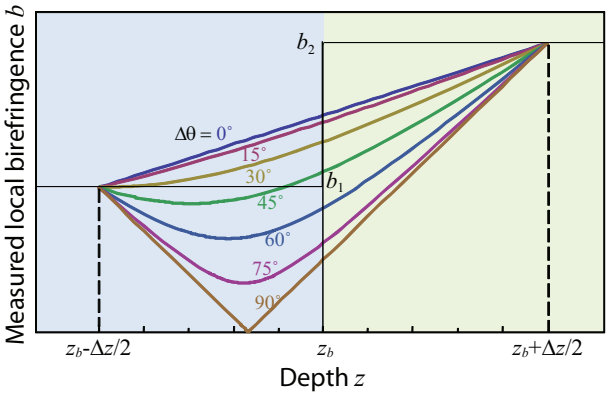

Fig. 13. Theoretical measured birefringence around the tissue boundary. It depends on the difference in the optic axis orientations of tissues $\Delta\theta$. b_1, b_2: Theoretical birefringences of tissues 1 and 2, respectively.

where b and θ are birefringence and optic axis orientation of each tissue located from z_u to z_d, respectively, and $\mathbf{R}$ is a rotation matrix.

The accumulated round-trip Jones matrices measured at the depths of z_1 and z_2 can be described as follows:

$$\mathbf{J}_T(z_1) = \mathbf{J}_1^T(z_{\text{surf}}, z_1)\mathbf{J}_1(z_{\text{surf}}, z_1) \tag{46}$$

$$\mathbf{J}_T(z_2) = \mathbf{J}_1^T(z_{\text{surf}}, z_b)\mathbf{J}_2^T(z_b, z_2)\mathbf{J}_2(z_b, z_2)\mathbf{J}_1(z_{\text{surf}}, z_b), \tag{47}$$

where z_{surf} is the depth of the sample surface and z_b is the depth of the boundary between two tissues. The local single-trip phase retardation $r(z_1, z_2)$ will be measured by applying the matrix trace method for $\mathbf{J}_T(z_2)\mathbf{J}_T^{-1}(z_1)$. Then, measured birefringence will be

$$b'(z) = \frac{r(z-\Delta z/2, z+\Delta z/2)}{2k_0\Delta z}$$

$$= \begin{cases} b_1 & (z \le z_b - \frac{\Delta z}{2}) \\ \frac{\cos^{-1}\left[\left|\cos\left(\Delta b k_0 z - \frac{1}{2} b_s k_0 \Delta z\right)\cos^2(\Delta\theta) + \cos\left(b_s k_0 z - \frac{1}{2}\Delta b k_0 \Delta z\right)\sin^2(\Delta\theta)\right|\right]}{k_0\Delta z} & (z_b - \frac{\Delta z}{2} < z < z_b + \frac{\Delta z}{2}) \\ b_2 & (z \ge z_b + \frac{\Delta z}{2}) \end{cases} \tag{48}$$

where $z = (z_2 + z_1)/2$ is the central depth of the measured local tissue. $b_s = b_1 + b_2$ and $\Delta b = b_1 - b_2$ are the sum and difference of the tissue birefringence, respectively. $\Delta\theta = \theta_1 - \theta_2$ is the difference between the optic axis orientations of two tissues.

The theoretically predicted measured results of the local birefringence around the boundary are shown in Fig. 13. As shown in the plot, the measured birefringence strongly depends on the difference in the optic axis orientation $\Delta\theta$. However, if one of the two tissues has no birefringence, the measured local birefringence does not depend on $\Delta\theta$ and is linearly increased or decreased. The results show that a dark line will appear near a boundary between two birefringent tissues at $\Delta\theta = 90^\circ$. A small axial separation can reduce only the axial range of an area with erroneous local birefringence due to the boundary effect, however, cannot reduce the magnitude of the error. As reduce the axial separation, the SNR of the birefringence measurement will be reduced.

#118929 - $15.00 USD Received 22 Oct 2009; revised 21 Dec 2009; accepted 23 Dec 2009; published 6 Jan 2010
(C) 2010 OSA

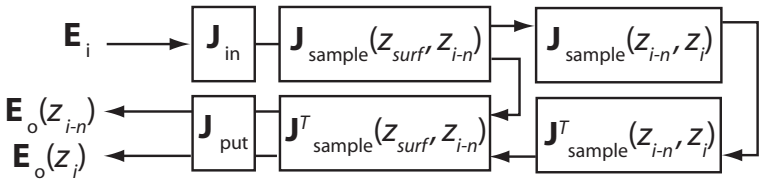

Fig. 14. Schematic diagram of the local birefringence measurement of the sample that exhibits diattenuation.

5.2. Input polarization states

In the experiments on PS-OCT, we introduced two orthogonal polarization states. The phase retardation error analysis in Sec. 3.1.1 shows that using two orthogonal polarization states is the most appropriate way from the point of view of phase retardation error due to low signal-to-noise ratio, at least for the Jones matrix method.

On the other hand, a combination of incident polarization states that are perpendicular to each other on the Poincaré sphere is used and the optimum set in PS-OCT imaging using Stokes-vector method [27, 34–36].

This dissimilarity maybe arise from the different degrees of freedom between the Jones matrix and Stokes-vector methods [37].

5.3. Free-space Jones matrix OCT for cumulative phase retardation measurement

In the case of phase retardation (not local) measurement by using free-space PS-OCT, either the reference measurement is not required or it need not be measured simultaneously with the sample measurement. Since the incident polarization states and polarization properties of optics are stable and can be known, the polarization properties of the sample can be directly obtained by substituting $\mathbf{E}_{\mathrm{in}}$ and system parameters into Eq. (7). SNRs of the calibration measurement can be very large with high reflectivity of a reference sample such as a mirror. Hence, $ESNR_{PR}^{-1} \approx SNR_1^{-1} + SNR_2^{-2}$ However, the phase difference ψ should be obtained to obtain the Jones matrix of the sample [17].

6. Conclusion

The Jones matrix OCT has been generalized, and its performances are investigated. A comparison of phase retardation calculation methods reveals that the diagonalization method exhibits a slightly better phase retardation accuracy and lower phase retardation error than the matrix trace method at low $ESNR_{PR}$ values. In either case, low $ESNR_{PR}$ will significantly increase the error and reduce the accuracy of phase retardation. A local birefringence imaging is described with the generalized Jones matrix OCT. Local birefringence imaging has been applied to biological tissues. A large axial separation between two measurement points increases the contrast of local birefringence images.

Appendix A. Diattenuation of the sample

The diattenuation of tissues does not cause phase retardation error in the diagonalization method, and the local relative-attenuation can be measured. However, retardation error will be caused in the unitary transform method [16], matrix trace method [Eq. (19)], and the quaternion method [11]. Here, the effect of the existence of diattenuation in a sample is investigated for the diagonalization and matrix trace methods by numerical simulations, and the latter is theoretically considered.

#118929 - $15.00 USD Received 22 Oct 2009; revised 21 Dec 2009; accepted 23 Dec 2009; published 6 Jan 2010
(C) 2010 OSA

The sample with diattenuation and its Jones matrix are modeled as shown in Fig. 14. Then, the measured Jones matrices at the front and back boundaries of the local tissue are

$$\mathbf{J}(z_{i-n-1}) = \mathbf{J}_{\text{out}}\mathbf{J}_{\text{S}}^{T}(z_{\text{surf}},z_{i-n-1})\mathbf{J}_{\text{S}}(z_{\text{surf}},z_{i-n-1})\mathbf{J}_{\text{in}} \quad (49)$$

$$\mathbf{J}(z_{i}) = \mathbf{J}_{\text{out}}\mathbf{J}_{\text{S}}^{T}(z_{\text{surf}},z_{i-n-1})\mathbf{J}_{\text{S}}^{T}(z_{i-n},z_{i})\mathbf{J}_{\text{S}}(z_{i-n},z_{i})\mathbf{J}_{\text{S}}(z_{\text{surf}},z_{i-n-1})\mathbf{J}_{\text{in}}. \quad (50)$$

The operation of the local Jones matrix measurement provides

$$\mathbf{J}(z_i)\mathbf{J}^{-1}(z_{i-n-1}) = \mathbf{J}_D\mathbf{J}_R\mathbf{J}_{\text{S}}^{T}(z_{i-n},z_i)\mathbf{J}_{\text{S}}(z_{i-n},z_i)\left(\mathbf{J}_R\right)^{-1}\left(\mathbf{J}_D\right)^{-1}\mathbf{J}_{\text{out}}^{-1}, \quad (51)$$

where the Jones matrix of the system from the local site to the detector $\mathbf{J}_{\text{out}}\mathbf{J}_{\text{S}}^{T}(z_{\text{surf}},z_{i-n-1})$ has been decomposed into the diattenuator $\mathbf{J}_D$ and retarder $\mathbf{J}_R$. By substituting $\mathbf{J}_D = \mathbf{J}_U^{T}[P_1,0;0,P_2]\mathbf{J}_U$ and $\mathbf{J}_{\text{S}} = \mathbf{R}(-\theta_s)[P_{s1}e^{ir/2},0;0,P_{s2}e^{-ir/2}]\mathbf{R}(\theta_s)$ into Eq. (51), it can be rewritten as

$$\mathbf{J}(z_i)\mathbf{J}^{-1}(z_{i-n-1}) = \mathbf{J}_{U1}\begin{bmatrix}P_1 & 0\\ 0 & P_2\end{bmatrix}\mathbf{J}_{U2}\begin{bmatrix}P_{s1}e^{ir/2} & 0\\ 0 & P_{s2}e^{-ir/2}\end{bmatrix}\mathbf{J}_{U2}^{-1}\begin{bmatrix}P_1 & 0\\ 0 & P_2\end{bmatrix}^{-1}\mathbf{J}_{U1}^{-1}, \quad (52)$$

where

$$\mathbf{J}_{U1} = \mathbf{J}_U^{T} \quad (53)$$

$$\mathbf{J}_{U2} = \mathbf{J}_U\mathbf{J}_R\mathbf{R}(-\theta_s) \quad (54)$$

are unitary matrices. P_1, P_2, and θ_P are the transmittances of eigenpolarization states and the fast axis orientation above the local tissue, and P_{s1}, P_{s2}, and θ_s are double-pass transmittances of eigenpolarization states and the fast axis orientation of the local tissue.

Here we define $\mathbf{J}_{U2}$ as a general unitary matrix form, i.e.,

$$\mathbf{J}_{U2} = \begin{bmatrix}e^{i\alpha/2} & 0\\ 0 & e^{-i\alpha/2}\end{bmatrix}\begin{bmatrix}\cos(\beta/2) & \sin(\beta/2)\\ -\sin(\beta/2) & \cos(\beta/2)\end{bmatrix}\begin{bmatrix}e^{i\gamma} & 0\\ 0 & e^{-i\gamma}\end{bmatrix}. \quad (55)$$

Then, the measured phase retardation by using the matrix trace method is theoretically obtained as

$$r_m = 2\cos^{-1}\left[\frac{\cos^2\frac{r}{2}+\frac{1-d}{1+d}\sin^2\frac{r}{2}}{\sqrt{2}\sqrt{\frac{1}{1+d}+\left\{\frac{1+D^2}{2(1-D^2)}\left[\frac{1-d}{1+d}\cos^2\frac{r}{2}+\sin^2\frac{r}{2}\right]-\frac{d}{1+d}\sin^2\frac{r}{2}-\frac{1-d}{2(1+d)}\right\}\sin^2\beta}}\right], \quad (56)$$

where $d = \sqrt{1-D_s^2}$. D_s and D are diattenuations:

$$D = \frac{P_1^2-P_2^2}{P_1^2+P_2^2} = \tanh\varepsilon \quad (57)$$

$$D_s = \frac{P_{s1}^2-P_{s2}^2}{P_{s1}^2+P_{s2}^2} = \tanh\varepsilon_s, \quad (58)$$

where ε and ε_s are relative-attenuations of the superior part and local tissue.

The retardation error due to diattenuations occurs if β is non-zero. Here β means the relative angle between the optic axes of the local tissue and above it.

Figure 15 shows the comparison of the phase retardation error due to the diattenuation of superior tissues $\mathbf{J}_D$. In Fig. 15, the horizontal axis is plotted by the relative-attenuation $\varepsilon =$

#118929 - $15.00 USD Received 22 Oct 2009; revised 21 Dec 2009; accepted 23 Dec 2009; published 6 Jan 2010
(C) 2010 OSA

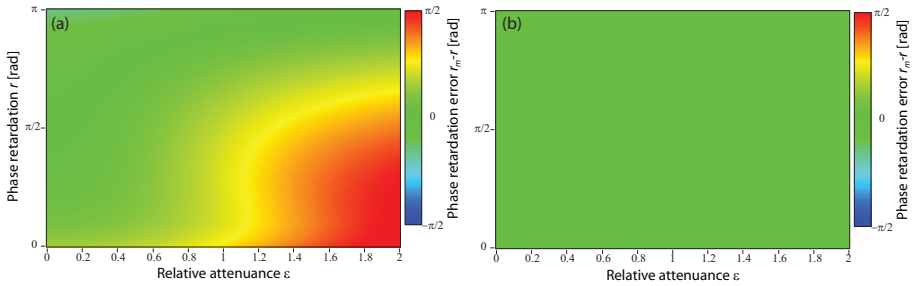

Fig. 15. Phase retardation error due to the diattenuation above the local tissue. The numerical simulation results of (a) Eq. (56) and (b) the diagonalization method. $\beta = \pi/2$ and $\varepsilon_S = 0.5$.

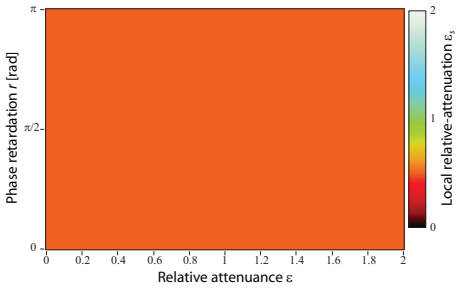

Fig. 16. Numerical simulation of the measured local relative-attenuation ε_s by using the diagonalization method. ε_s is set to be 0.5.

$\tanh^{-1} D$ [22], since it is convenient for depth-resolved polarimetry. The numerical simulation results of the diagonalization method show no phase retardation error due to the diattenuations [Fig. 15(b)]. On the other hand, the matrix trace method exhibits phase retardation error at large relative-attenuations [Fig. 15(a)]. The relative-attenuation ε can be significantly large if anisotropic tissues such as the collagen fiber and muscles are stacked in thick block and its orientation is aligned. Several diattenuations of biological tissues are measured [12, 16, 17, 22]. According to these results, the relative-attenuation per depth is less than 1 mm^{-1}. Unless the volume of well-aligned fibrous tissues is thicker than 500 μm, the error in the phase retardation due to the diattenuation will be less than $\sim 4^\circ$. In the case of low diattenuation of the sample, the matrix trace method will be applicable to local phase retardation measurement.

Figure 16 shows the numerical simulation of local relative-attenuation measurements with the diagonalization method. It shows that the diagonalization method can be used to measure the local diattenuation.

Acknowledgment

The authors acknowledge valuable comments from Prof. B. Cense, Utsunomiya University. This research is supported by a Grant-in-Aid for Scientific Research 18360029 from the Japan Society for the Promotion of Science (JSPS) and Japan Science and Technology Agency.

#118929 - $15.00 USD Received 22 Oct 2009; revised 21 Dec 2009; accepted 23 Dec 2009; published 6 Jan 2010
(C) 2010 OSA